Catalysis Communications 182 (2023) 106738

Contents lists available at ScienceDirect

Catalysis Communications

journal homepage: www.elsevier.com/locate/catcom

In situ impregnated Ni/Al_2O_3 catalysts prepared by binder jet 3D printing using nickel nitrate-containing ink

Hanh My Bui [a,b], Tim Kratky [a,b], Insu Lee [a,b], Rachit Khare [a,b], Max Hiller [a,b], Steffen Wedig [a,b], Sebastian Günther [a,b], Olaf Hinrichsen [a,b,*]

[a] TUM School of Natural Sciences, Technical University of Munich, Lichtenbergstraße 4, 85748 Garching, Germany
[b] Catalysis Research Center, Technical University of Munich, Ernst-Otto-Fischer-Straße 1, 85748 Garching, Germany

ARTICLE INFO

Keywords:
Binder jetting
Additive manufacturing
Heterogeneous catalysis
Nickel catalyst
Supported catalyst
Wet impregnation
Nickel aluminate spinel

ABSTRACT

The binder jetting printing technique enables in situ impregnation of alumina using a $Ni(NO_3)_2$-containing ink (NI), facilitating omission of impregnation. NI was compared to wet impregnation (WI). Full characterization by quasi-in situ XPS, XAS and TPR revealed the presence of Ni as $NiAl_2O_4$ spinel. TPR analysis identified surface NiO and $NiAl_2O_4$ species with facilitated reduction by NI, in addition to the respective species in bulk form. Post-processing affects active site accessibility by coverage. 3D printing limited the Ni loading, but XPS revealed higher metal dispersion by NI. CO_2 hydrogenation confirmed active Ni/Al_2O_3 catalysts with enhanced activity by NI.

1. Introduction

Supported catalysts are the most common form of heterogeneous catalysts prepared by depositing small crystallites of an catalytically active component on a porous support [1]. The method of catalyst immobilization influences the catalyst performance since the resulting metal-support interaction controls crucial properties such as active phase dispersion and long-term stability. Apart from co-precipitation and the sol–gel method [2], wet or incipient wetness impregnation are the most relevant and frequently used preparation methods. In this process, the support is immersed in the impregnation solution, dried and subsequently reduced by calcination and/or reduction [1]. Numerous studies have extensively explored and compared the influence of mentioned catalyst immobilization methods on metal speciation, particle size, dispersion, reducibility and associated catalyst activity and deactivation behavior [3–8] and they have proven correlations between the preparation technique and catalyst performance.

The usage of powdered catalysts is a standard approach for most academic questions. However, catalyst shaping is essential for the application of heterogeneous catalysts on a technical scale, especially in fixed bed reactors. Good abrasion resistance, mechanical durability, ease of separation from the reactants, and decreased pressure drop inside the reactor necessitate forming techniques such as agglomeration, spray granulation, tableting or extrusion to enlarge the size of the catalyst [9]. The latter two methods are well-established and represent the most commonly used catalyst shaping techniques on an industrial scale [10]. Related thereto, the active phase distribution in a formed catalyst (e.g. uniform, egg-shell, egg-white, egg-yolk) influences the performance of a catalytic reactor by varying accessibility of the active sites [11–13].

Based on the growing number of publications, additive manufacturing (AM) or 3D printing has been increasingly exploited for catalyst shaping to meet the growing interest in intensification of industrial and environmental heterogeneous catalysis [14–19].

In general, catalysts can be 3D printed *indirectly* by manufacturing a template with a polymeric 3D printer. This mold is filled with a paste of ceramics or catalytic material and thermally treated to burn off the polymer to expose the monolithic catalyst structure [20–22]. *Direct* printing involves 3D printing without removable templates, namely printing of catalyst support for further impregnation or incorporation of the active phase into the printing feedstock.

Several printing techniques from the plethora of AM technologies available nowadays have been applied for printing of predominantly monolithic catalyst geometries. Direct Ink writing (DIW/robocasting) or fused deposition modeling (FDM) are extrusion-based principles and most commonly used due to their relatively intuitive material design, especially regarding processing of metal oxide feedstock [23–28]. Powder-based techniques oftentimes require more detailed material and

---

* Corresponding author at: TUM School of Natural Sciences, Technical University of Munich, Lichtenbergstraße 4, 85748 Garching, Germany.
E-mail address: olaf.hinrichsen@ch.tum.de (O. Hinrichsen).

https://doi.org/10.1016/j.catcom.2023.106738
Received 7 June 2023; Received in revised form 20 July 2023; Accepted 22 July 2023

process development. Selective laser melting (SLM) has been used to generate monolithic metal frameworks which are subsequently wash-coated with catalytically active material [29–31]. The printing technique used in this paper is binder jetting (BJ), a powder-based AM technique. BJ allows for fabrication of highly porous ceramic bodies for catalysis [32,33] while enabling relatively complex structures without support structures.

Previous studies on catalyst manufacturing strategies utilizing binder jetting exist. One of them includes printing of the metal oxide support which has to be followed by impregnation with the active phase [33]. The second strategy integrates powdery co-precipitated catalyst precursor into the printing powder [34]. This paper explores the preparation of binder jet 3D printed Ni/Al_2O_3 catalysts by deposition of nickel containing ink onto Al_2O_3 powder, therefore resembling impregnated Ni/Al_2O_3 catalysts regarding their physicochemical properties. The nickel precursor is dissolved in the printing liquid which is deposited selectively and layer-by-layer onto the alumina print bed by the inkjet print head. This method constitutes an in situ impregnation of the support during 3D printing, thus omitting the successive impregnation step. Due to the ejection of fine liquid droplets, this method could influence the morphology of the active phase applied onto the support surface. Combined with the extensive freedom for catalyst forming provided by AM, the new manufacturing strategy could add improvements to conventional catalyst preparation procedures by offering tailor-made catalyst shapes coupled with effective active phase distribution.

2. Experimental

2.1. Catalyst preparation by binder jetting with Ni containing ink

The general manufacturing strategy is based on a previously presented method for alumina supports printed by binder jetting [33]. Fig. 1 depicts the setup of the printer used for catalyst printing. The powder reservoir and the print platform were filled with the printing powder consisting of 73 wt.% bayerite Pural BT (Sasol Chemicals, USA), 7 wt.% Actilox S40 (Nabaltec AG, Germany), and 20 wt.% of the solid binder polyvinyl pyrrolidone (PVP) Sokalan K17P (BASF SE, Germany). The aqueous printing liquid consisted of distilled water, 10 wt.% isopropyl alcohol, 10 wt.% 1,4-butanediol and varying amounts of nickel nitrate $Ni(NO_3)_2{\cdot}6H_2O$ (all purchased from Merck KGaA, Germany), depending on the desired Ni loading. The powder was selectively bound layer-by-layer with the Ni containing printing liquid which is conveyed from an ink reservoir by a drop-on-demand (DOD) shear-mode piezo inkjet printhead (508GS, Seiko Instruments GmbH, Japan) via hydrostatic pressure. After printing, the light green Ni nitrate impregnated alumina supports (diameter $d = $ height $h = 6$ mm) were transferred to a drying oven to cure the PVP binder for at least 2 h (Fig. 2a) at 75 °C. Subsequently, the green parts were debindered in a muffle furnace for 3 h at 600 °C in order to fully remove the binder, resulting in highly porous debindered samples. Subsequently, an aqueous boehmite slurry was slowly dripped onto the debindered parts until pore saturation for additional particle introduction by infiltration. Another calcination step (600 °C, 3 h) followed, resulting in a mechanically stable 3D printed nickel catalyst (Fig. 2b).

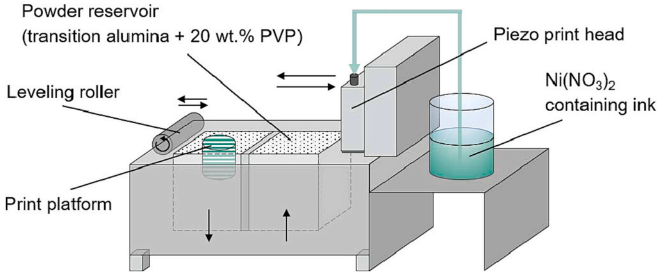

Fig. 1. Schematic of the binder jetting printer used in this study.

2.2. Catalyst preparation by wet impregnation

Wet impregnated Ni catalysts were prepared using binder jet printed cylindrical alumina supports which were subsequently impregnated in an excess of nickel nitrate solution of adequate concentration. The Al_2O_3 carriers were printed using the same powder mix as described in Section 2.1 but using ink without any nickel nitrate. The detailed manufacturing procedure for porous alumina supports is described in a previous study [33]. Printed supports were immersed in an aqueous solution of Ni $(NO_3)_2{\cdot}6H_2O$ with varying Ni concentration for 2 h under constant stirring. The liquid was then fully removed using a rotary evaporator. After drying, the precursors were calcined in a muffle furnace (450 °C/ 600 °C, 6 h).

2.3. Sample nomenclature

Table 1 summarizes all samples characterized in this study. The novel nickel ink deposition 3D printing method (NI) was compared to the well-established wet impregnation (WI) method. The letters “d” and “i” denote debindered or infiltrated samples, respectively. The precursors were either calcined at 450 °C (c450) or 600 °C (c600) and reduced with H_2 at 480 °C (r480) or 600 °C (r600).

2.4. Catalyst characterization

2.4.1. Elemental analysis

Ni loading was determined by graphite furnace atomic absorption spectroscopy (GFAAS), using an ICE 3500 AAS by Thermo Fisher Scientific. Ground samples were dissolved in boiling, fuming sulfuric acid and diluted with distilled water. Subsequently, 5–20 μL of the diluted sample was inserted into the GFAAS and analyzed.

2.4.2. Compressive test

Mechanical stability of the 3D printed catalysts were tested with a hardness tester with integrated size measurement (MultiTest 50, Dr. Schleuniger Pharmatron) by uniaxial compression test. Sample size for each measurement was 10. The tested geometries were cylinders measuring 6 mm in diameter and height. Testing direction was perpendicular to the cylinder axis, the bracket moving speed was set to 2 mm/s. The compressive strength σ_{comp} was calculated based on the fracture load F using the equation given by Timoshenko and Goodier [35].

$$\sigma_{comp} = \frac{2F}{\pi dh} \tag{1}$$

where d denotes the cylinder diameter and h its height.

2.4.3. Archimedes buoyancy method

Densities and void fractions of the printed and post-processed samples were acquired using the Archimedes buoyancy method according to DIN EN 623–2 [36,37]. Distilled water was chosen as the fluid. The sample was degassed at 25 mbar in a rotary evaporator at ambient temperature before distilled water was added, following repressurization to atmospheric pressure. For density calculations, the sample was weighed in its dry, water-impregnated and submerged state.

2.4.4. X-ray photoelectron spectroscopy and CO_2 hydrogenation activity

X-ray photoelectron spectra (XPS) were recorded on a Leybold-Heraeus LHS 10 spectrometer using a non-monochromatized Al K_α source (1486.7 eV). 3D printed cylindrical catalysts were ground prior to measurement. The obtained powders were pressed into cavities and measured as pellets (~50 mg). All spectra were recorded in an ultra-high vacuum chamber at a pressure below $5{\cdot}10^{-8}$ mbar. The analyzer was

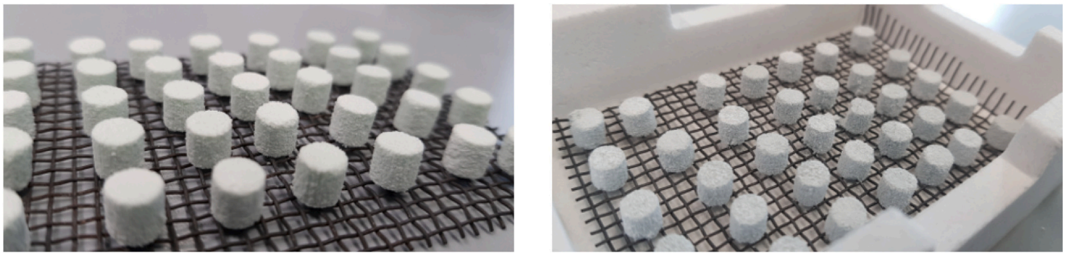

(a) Green part after after curing at 70 °C. Light green color indicates deposition of nickel nitrate ink on alumina powder.

(b) Calcined at 600 °C. Light blue coloration due to predominant conversion of Ni precursor to nickel aluminate spinel.

Fig. 2. Test cylinders at different processing stages printed by Ni ink deposition.

Table 1

Sample nomenclature of catalysts prepared by Ni ink deopsition (NI) and wet impregnation (WI) with respective nickel loading w_{Ni}, calcination T_{calc} and reduction Temperature T_{red}.

Sample	w_{Ni} (wt. %)[a]	T_{calc} (°C)	T_{red} (°C)	Preparation method
Calcined samples				
NI_d_c600	3.4	600	–	Ni ink deposition, debindered
NI_i_c600	2.5	600	–	Ni ink deposition, infiltrated
Reduced samples				
NI_d_c600_r480	3.4	600	480	Ni ink deposition, debindered
NI_d_c600_r600	3.4	600	600	Ni ink deposition, debindered
NI_i_c600_r480	2.5	600	480	Ni ink deposition, infiltrated
WI_c600_r480	1.6	600	480	Wet impregnation
WI_c450_r480	1.8	450	480	Wet impgrenation

[a] Determined by AAS.

operated at a constant pass energy of 100 eV leading to an energy resolution with a full width at half-maximum (FWHM) of ca. 1.1 eV. The energy scale of the spectra was corrected for sample charging by using the Al 2s signal at 120.0 eV.

Reduction of the catalyst samples (50 mbar H_2, 400 °C, 5 sccm, >2 h) and in situ CO_2 hydrogenation (2 mbar CO_2, 8 mbar H_2, 1 mbar Ar, 300 °C) were carried out in a preparation chamber directly attached to the XPS analysis chamber enabling sample transfers without exposing the catalyst to air. The composition of the gas phase was analyzed by a differentially pumped Pfeiffer Vacuum PrismaPro QMG 250 M3 quadrupol mass spectrometer which was operated at pressures below 10^{-6} mbar. The intensity of all traces were scaled to the intensity of Ar ($m/z = 40$) to account for volume contraction upon CO_2 hydrogenation. $m/z = 15$ was used as characteristic fragment for the partial pressure of CH_4. The intensity of $m/z = 28$ indicating the partial pressure of CO was corrected for the fraction resulting from CO_2 fragmentation by subtracting the intensity of $m/z = 44$ multiplied by the fragmentation ratio. The fragmentation ratio was determined by the intensity ratio of $m/z = 28$ to $m/z = 44$ in the initial feed gas as the entire $m/z = 28$ intensity is caused by CO_2 fragmentation only. Details of the experimental setup and the activity measurements are given in the Supplementary Material.

2.4.5. Ni K-edge X-ray absorption spectroscopy

Ni K-edge X-ray absorption spectroscopy (XAS) measurements were carried out on beamline P65 at PETRA III of DESY in Hamburg, Germany. Reduced samples were reduced ex situ at 480 °C or 600 °C. Furthermore, samples were kept under inert conditions after reduction and transferred to a glovebox, where the samples were ground and filled into a quartz capillary with a diameter of 2 mm. A double-crystal Si(111) monochromator was used to adjust the incident photon energy, and the spectra were recorded with ionization chambers in transmission and in total fluorescence yield using a passivated implanted planar silicon (PIPS) detector. ATHENA software was used for the background processing. XAS normalization followed standard protocol used within the Athena software [38].

2.4.6. Temperature programmed reduction

Temperature programmed reduction (TPR) was measured on a Micromeritics Autochem II analyzer equipped with a thermal conductivity detector (TCD). Pre-treatment by degassing at 300 °C for 2 h under inert gas flow had no influence on the TPR signals so that no outgassing was necessary. About 300 mg of sample was heated at a rate of 5 K/min until 1100 °C. 5 % H_2/Ar was used as reducing gas with a flow of 30 mL/min [39]. Evolving H_2O was frozen out in a cold trap using an isopropyl alcohol/liquid N_2 frigorific mixture.

3. Results

3.1. Proof of concept by preliminary printing tests

The feasibility of the Ni ink deposition method was verified by preliminary tests. Ni containing inks with varying molar concentrations of nickel nitrate were used as printing liquid and deposited on the alumina print bed (see Table 2). The final Ni loading can be adjusted by the concentration of nickel nitrate in the ink or the amount of deposited nickel ink during the printing process. Naturally, a higher concentration of $Ni(NO_3)_2$ in the printing liquid increases the final Ni loading w_{Ni} of the catalyst. However, the permitted ink pH range declared by the hardware manufacturer needs to be considered. The ink pH decreases with increasing nickel nitrate concentration so that the print head compatibility poses an upwards limitation regarding nickel salt concentration in the ink. Moreover, the liquid drop size generated by the print head as well as the required amount of ink for adequate powder bed saturation determines the final metal loading of the 3D printed catalyst.

Fig. 3 presents the results of compression tests for samples conducted after the debinding step and in their final state after second calcination. The compressive strength of debindered samples is low in general with values below 0.08 MPa since the evaporation of PVP leads to high porosity and voidage, decreasing the number and strength of contacting

Table 2

Molar nickel nitrate concentration $cNi(NO_3)_2$ of used ink, its pH, resulting Ni loading of the catalyst w_{Ni} and sample densities ρ after final post-processing.

$cNi(NO_3)_2$ (mol/L)	pH of ink	w_{Ni} (wt.%)	$\rho_{app,s}$ (g/cm^3)	ϵ_{open}
3.0	1.5	3.4	3.2	0.74
2.0	2.5	1.8	3.1	0.74
1.0	3.2	1.0	3.0	0.74
0.5	3.9	0.5	3.1	0.76

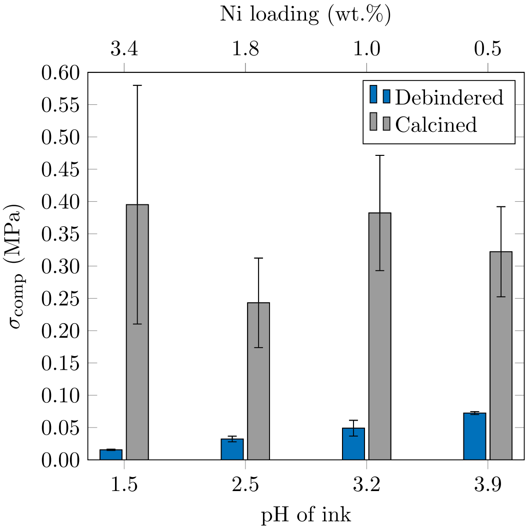

Fig. 3. Compressive strength σ_{comp} of debindered (blue) and calcined (gray) test cylinders for varying pH values of the Ni ink (see Table 2).

points between the alumina particles. However, their σ_{comp} indicates a trend towards increased mechanical stability with increasing pH of the ink. Therefore, we can infer that decreased ink pH impairs the binding ability of PVP to consolidate the green part, the unprocessed geometry formed immediately after 3D printing. After drip infiltration with boehmite slurry and subsequent calcination, compression strength increases significantly for all samples. Considering the relatively large standard deviation of σ_{comp} for calcined parts, the final mechanical stability is similar for all investigated samples, ranging between 0.24±0.07 MPa and 0.40±0.18 MPa. Therefore, the infiltration step is crucial for the binder jetting procedure and decisive for mechanical robustness and practical applicability of the catalyst inside a chemical reactor.

The catalytically relevant open porosity ϵ_{open} and the apparent solid density $\rho_{app,s}$ in dependence of the nickel nitrate concentration and the ink pH are tabulated in Table 2. $\rho_{app,s}$ is defined by the sample mass divided by the total volume of the solid including closed voids. $\rho_{app,s}$ and ϵ_{open} remain nearly constant throughout all four studied samples (Table 2), meaning that the catalytically accessible surface area is similar regardless of the pH of the ink. Thus, the NI method allows fabrication of catalysts with a consistent pore structure. Moreover, the porosity and specific surface area values agree with results determined in a previous study which introduced the basic catalyst support printing process this paper is based on [33] so that the reproducibility of the printing process is given. Results for the specific surface area can be taken from Table S1 in the Supporting Information.

3.2. XPS analysis

Fig. 4 displays the Ni 2p core level spectra of the catalysts synthesized by Ni ink deposition before (NI_d_c600) and after post-processing (NI_i_c600) as well as the samples obtained by conventional impregnation after calcination at 450 °C and 600 °C (WI_c450 and WI_c600, respectively). The intensity of the spectra is scaled to the Al 2s peak intensity as well as the Ni loading so that the intensity reflects the amount of Ni present on the sample surface. The binding energy of the Ni 2p main peak and its satellite is centered around 857.3 eV and 863.4 eV, respectively, regardless of the synthesis method and calcination temperature. Both binding energy and peak shape are characteristic for Ni^{2+} and expected for Ni/Al_2O_3 catalysts after calcination [8]. Drip infiltration of the printed catalysts with a boehmite slurry physically covers the Ni surface species, leading to an attenuation of the Ni 2p signal as observed by the surface sensitivity of XPS. Thus, the intensity of the Ni 2p core level of NI_d_c600 exceeds the one of NI_i_c600 by a factor of almost 2, indicating an influence of the AM post-processing on the calcined samples (see Fig. 5a). The Ni ink deposition method reveals an up to three times higher Ni 2p intensity compared to conventional Ni wet impregnation after calcination at the same conditions (see Fig. 5a). The increased signal intensity proves a higher Ni coverage on the oxidic support structure. As intensity correction for slightly differing metal loadings was executed, a higher coverage of Ni can be derived from smaller Ni oxide particles and, thus, a higher metal oxide dispersion on the catalyst surface. The increased Ni dispersion might be introduced by the binder jetting 3D printing process as small ink droplets are generated when Ni nitrate solution is jetted through the fine nozzles of the printhead.

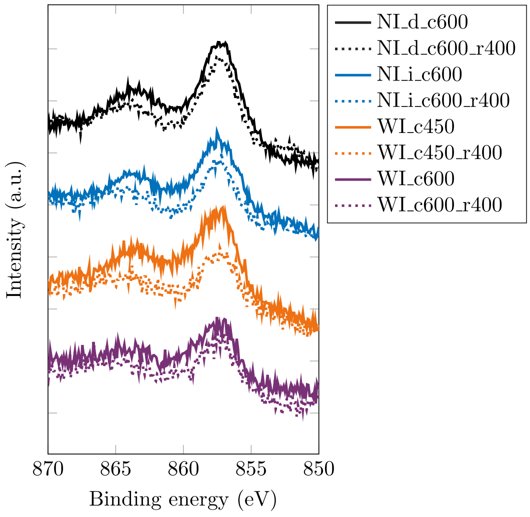

Fig. 4. XPS Ni 2p spectra of NI_d (debindered), NI_i (infiltrated), and WI samples, calcined at 450 °C (c450) and 600 °C (c600, solid line) and reduced at 400 °C (r400, dotted line).

Surprisingly, Fig. 5a also shows that lowering the calcination temperature from 600 °C to 450 °C results in a three times higher Ni 2p intensity for the WI catalysts. Note that a calcination temperature of 600 °C is required for entire removal of the binder materials in NI samples and cannot be decreased [33]. As the preparation by wet impregnation creates $Ni(NO_3)_2$ particles on the alumina support, calcination converts the nitrate to an oxide. Although sintering of NiO particles upon calcination at a higher temperature cannot be ruled out entirely, the lower Ni coverage on the surface at elevated temperatures is likely explained by Ni bulk diffusion. The formation of $NiAl_2O_4$ spinel

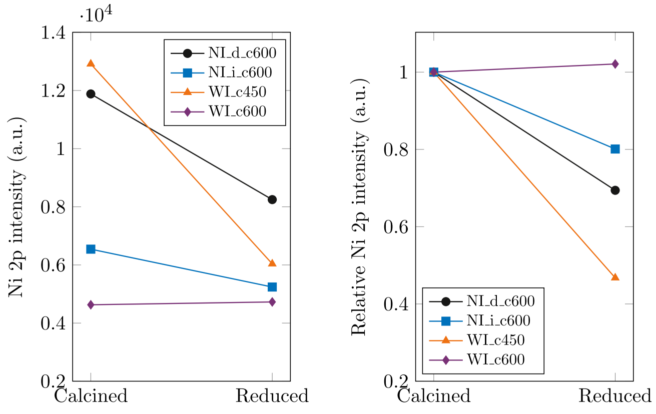

(a) Ni 2p intensity

(b) Relative Ni 2p intensity

Fig. 5. Ni 2p intensities of calcined and reduced samples.

structures instead of NiO/Al_2O_3 is thermodynamically favored [40]. This could occur by diffusion of nickel and oxygen ions through the aluminate [41], counterdiffusion of NiO and Al_2O_3 through the spinel layer or counterdiffusion of Ni^{2+} and Al^{3+}[42]. Huang et al. reported on the formation of different nickel species as a function of the Ni loading in wet impregnated Ni/Al_2O_3 systems and found the exclusive formation of $NiAl_2O_4$ at weight loadings below 1 % while both NiO and $NiAl_2O_4$ are formed at higher Ni loadings [3]. This goes in line with our spectroscopic results; the fairly low Ni loading of 1.7 wt.% on average favors predominant formation of $NiAl_2O_4$. The preceding diffusion of Ni into the alumina structure reduces the amount of Ni surface species leading to a strongly diminished Ni 2p signal. At lower calcination temperatures, Ni bulk diffusion is kinetically hindered so that the metal oxide remains on the catalyst surface as observed by a significantly higher Ni 2p intensity after calcination at 450 °C. Those findings are supported by quasi-in situ XPS analysis after reduction of all samples in 50 mbar of hydrogen at 400 °C (see dotted lines in Fig. 4).

While Ni 2p peak shape and intensity remain constant for the WI_c600 catalyst, the intensity of WI_c450 is decreased by $\sim$55% compared to the calcined state (see Fig. 5b). The low amount of Ni species on the WI_c600 surface is presumably incorporated in a nickel aluminate spinel structure and, hence, hard to reduce. In contrast, Ni^{2+} species on the WI_c450 surface are strongly affected by the reductive treatment as can be deduced from the change in signal intensity. However, no metallic Ni 2p component is found in XPS. This might originate from the formation of metallic particles which do not contribute to the Ni 2p peak intensity if they cover a negligible surface fraction of the support. It is well known that reduction of co-precipitated nickel aluminum mixed oxides reveals metallic nanoparticles on a Ni-poor mixed oxide surface [43,44]. As the Ni^0 particles contribute less to the overall surface area than homogeneously distributed Ni^{2+} in the mixed oxide, a lower Ni 2p intensity is observed. Considering the loss in Ni 2p intensity during reduction of WI_c450, the expected intensity of the metallic component might be below the detection limit due to the low Ni loading.

Reduction of NI_d_c600 and NI_i_c600 leads to a decrease of the Ni 2p signal of 30% and 20%, respectively (see Fig. 5b), which corresponds to the portion of Ni^0 particles in coexistence with Ni^{2+} species. Since the Ni^{2+} species exclusively cause the Ni 2p photoemission yield, the XPS data show that in both cases, the Ni^{2+} present at the catalyst surface cannot be reduced completely under typical activation conditions used for Ni/Al_2O_3 catalysts. This confirms the formation of nickel aluminate spinel structures upon calcination at 600 °C, which are barely reducible (see TPR studies discussed in Section 3.4 further below). The higher reducibility of the samples before AM post-processing (NI_d_c600) corroborates blocking of the Ni species by infiltration with boehmite slurry. Covering the surface Ni by alumina inhibits the accessibility by the reductive gas atmosphere and, thus, formation of metallic Ni particles significantly. Nonetheless, 20 % of the Ni is still reduced under mild conditions, proving the successful fabrication of Ni/Al_2O_3 catalysts by the novel Ni ink deposition method.

3.2.1. CO_2 hydrogenation activity

After reducing the NI and WI samples, their catalytic activity for the hydrogenation of CO_2 was studied by converting a gas mixture of CO_2 and H_2 ($p = 10$ mbar, $CO_2/H_2 = 1/4$) at 300 °C in a batch-type reaction cell (for experimental details, see Supporting Information). The mass traces of the reaction products CH_4 and CO are depicted in Fig. 6. The methanation rate is slow for all analyzed samples while CO is the main product. Comparison with a co-precipitated Ni-Al benchmark catalyst reveals that the most active 3D printed catalyst exhibits a CO_2 methanation rate that is more than two orders of magnitude slower (see Fig. S4 in Supporting Information). Wet impregnated WI_c600 shows negligible activity in general, producing almost no CH_4 (Fig. 6a) and and only a minor amount of CO (Fig. 6b). The activity of the corresponding WI_c450 is significantly higher, which conforms with the XPS findings. The higher amount of surface Ni and enhanced reducibility improve the catalytic activity of the wet impregnated sample calcined at lower temperatures. Catalysts fabricated with Ni ink deposition yield the highest activities. While the debindered sample NI_d_c600 favors CH_4, the selectivity is driven towards CO after infiltration with boehmite slurry and subsequent calcination. Based on the XPS surface analysis, this might originate from a lower Ni coverage combined with an inferior reducibility after AM post-processing. The CO/CH_4 selectivity and reaction pathway have been proven to be highly sensitive to the Ni particle size or dispersion [45]. Wu et al. [46] studied the CO_2 hydrogenation on Ni/SiO_2 catalysts with a Ni loading of 0.5 wt.% and 10 wt.% and revealed that the selectivity towards methane is significantly enhanced on large Ni particles (high Ni loading), whereas CO formation was preferred at low Ni loadings. Co-adsorbed CO_2 and H_2 on Ni^0 particles form the key intermediate *m*-HCOO which is subsequently decomposed to CO and may follow a consecutive reaction pathway to CH_4. However, due to the low coverage of the active centers by H_2 at low metal loadings, CO formation is favored [46,47].

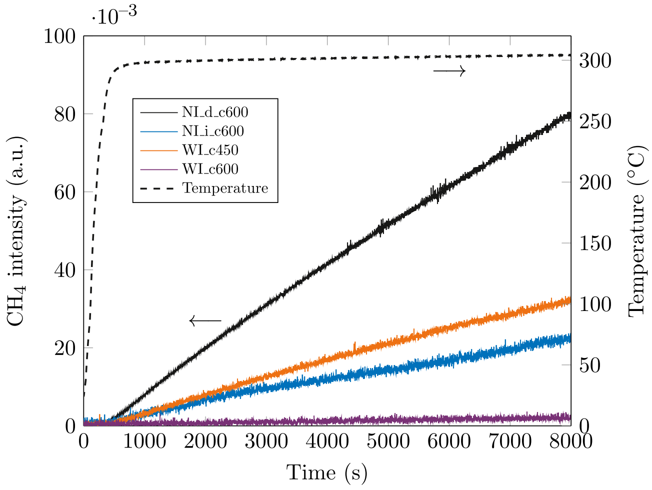

(a) CH_4 signal intensity.

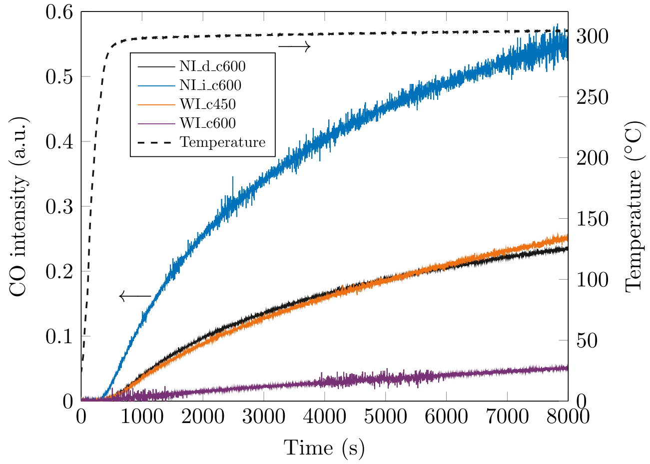

(b) CO signal intensity.

Fig. 6. Quadrupol mass spectrometry signal intensities of the CO_2 hydrogenation reaction products methane and carbon monoxide. Feed gas composition: $CO_2/H_2/Ar = 2/8/1$.

3.3. Ni K-edge XAS analysis

Samples reduced at two different temperatures (480 °C and 600 °C) were analyzed regarding the chemical form and oxidation state of Ni to investigate the presence of nickel aluminate by 3D printing. Furthermore, the preparation methods NI and WI were compared as well as the influence of post-processing.

3.3.1. Calcined state

Ni K-edge XANES spectra of the calcined samples show a pre-edge peak at around 8335 eV (see exemplary spectrum Fig. 7a, all other spectra see Fig. S1), which is attributed to dipole forbidden 1s to 3d transitions, thus confirming the Ni^{2+} character of the sample [48,49]. Furthermore, the white line area strongly resembles that of the reference samples, indicating the dominant presence of nickel as Ni^{2+} [50]. The pre-edge feature as well as the edge energy of all calcined samples notably match with $NiAl_2O_4$, substantiating the surface analysis by XPS that not only the catalyst surface but also the bulk material mainly contains Ni aluminate species.

Fig. 7a presents the Ni K-edge XANES of NI_i_c600. The spectra of the remaining calcined samples NI_d_c600, WI_c600 and WI_c450 can be accessed through the Supporting Information (Fig. S1). The strong nickel aluminate character of all samples indicates that calcination at 450 °C as well as 600 °C is sufficient to induce growth of nickel aluminate spinel due to incorporation of nickel particles into the alumina lattice. Despite the overall similarity to $NiAl_2O_4$, the effect of calcination temperature is visible comparing the samples WI_c450 and WI_c600 (see Fig. S1c and S1d, respectively). WI_c450 shows a more pronounced NiO character at about 8348 eV, distinguishing it from the wet impregnated sample calcined at 600 °C (WI_c600) which matches with Ni aluminate across the entire energy range. This observation suggests that at a calcination temperature of 450 °C NiO is preferably formed than at 600 °C and T_{calc} affects the Ni speciation on the catalyst support surface.

Fig. 8 shows the k^2-weighted Fourier-transformed EXAFS at the Ni K-edge of calcined NI_i_c600 and its reduced form NI_i_c600_r480. Both samples show a prominent peak at ca. 1.5 Å, which corresponds well to backscattering from oxygen, directly bonded to Ni. This feature is in good agreement for first shell M-O metal oxide bonds, which are expected to be located between 1–2 Å. Furthermore, the prominent peak at ca 2.5 Å is associated to Ni-Ni scattering paths of metal oxides. The mentioned features of calcined NI_i_c600 show approximately the same positions compared to the NiO reference, reconfirming a Ni^{2+} character of the calcined samples.

3.3.2. Reduced state

All calcined samples were reduced ex situ at 480 °C and kept under inert conditions afterwards. NI_d_c600 was additionally reduced at 600 °C to examine the effect of reduction temperature. Ni foil was the metallic Ni standard and the corresponding calcined sample acted as the fully oxidized reference sample. Fig. 7b presents an exemplary Ni K-edge XANES spectrum of a reduced sample. Remaining plots are displayed in the Supporting Information (Fig. S2). The extent of reduction to metallic nickel is low in general since the character of the calcined sample is mostly maintained, as seen in Figs. S2a-e. The existence of the pre-edge feature at 8333 eV for all samples confirms an incomplete reduction of Ni^{2+} to metallic nickel which does not display this pre-edge peak.

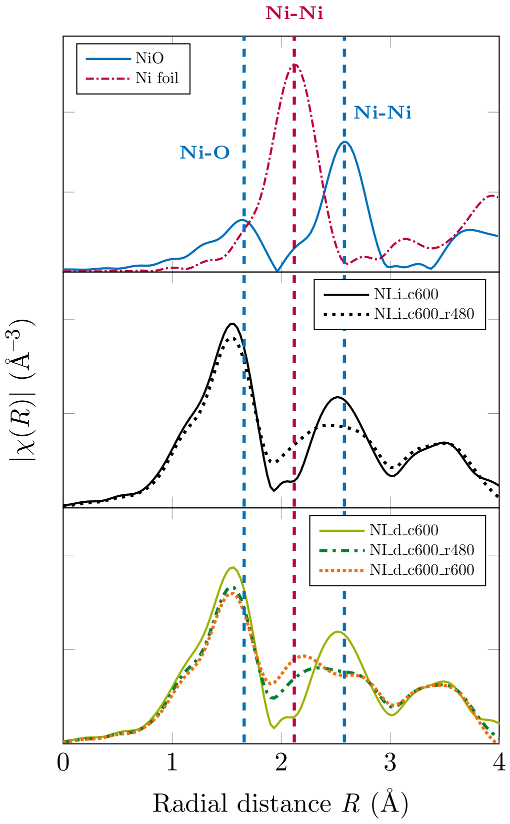

Fig. 8. Comparison of k^2-weighted Fourier-transformed EXAFS of different NI prepared samples at the Ni K-edge. Bottom: Debindered samples reduced at 480 °C and 600 °C. Middle: Infiltrated samples, calcined and reduced. Top: References.

Although XANES shows small signs of reduced Ni, the k^2-weighted Fourier-transformed EXAFS at the Ni K-edge of different NI prepared samples exhibits different features. After reduction, NI_i_c600_r480 shows a decrease and broadening of the Ni-Ni scattering paths, see Fig. 8. The broadening is interpreted as partial reduction of Ni(II) species to metallic Ni. As seen in Fig. 8, Ni metal foil shows the first shell Ni-Ni at

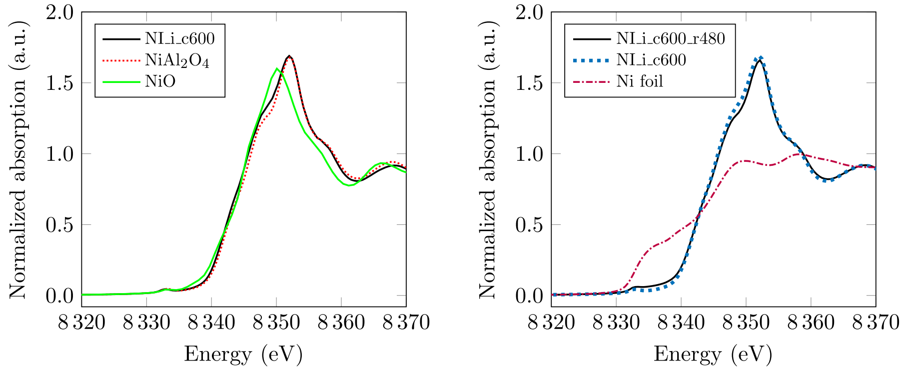

(a) NI_i_c600

(b) NI_i_c600_r480

Fig. 7. Ni K-edge XANES spectrum of (a) NI_i_c600 (infiltrated, calcined at 600 °C) and references $NiAl_2O_4$ and NiO and (b) NI_i_c600_r480 (reduced at 480 °C) and corresponding references NI_i_c600 and Ni foil.

ca. 2.1 Å. In fact, NI_i_c600_r480 exhibits a broadening towards 2.1 Å, indicating a certain extent of reduction to metallic nickel. This phenomenon is even more distinct for the sample NI_d_c600 which is also illustrated in Fig. 8. Upon increase of reduction temperature from 480–600 °C, the broadened Ni-Ni peak of the metal oxide shifts about 0.7 Åtowards a distinct Ni-Ni feature at ca. 2.1 Å, corroborating that reduction takes place.

3.4. *TPR analysis*

Fig. 9a compares the normalized H_2 consumption by TPR of two Ni catalysts prepared by Ni ink deposition, one being debindered and the other infiltrated (d/i). Degrees of reduction ranging from 95–100 % indicate that TPR conducted until 1100 °C fully reduces all present Ni species to metallic Ni^0 (see R_{TPR} in Table 3).

Both NI samples reveal four reduction peaks with the first and the last two ones overlapping, thus representing two regions. NiO contributes to the first two peaks and Ni aluminate species are associated with the last two peaks, corroborating previous findings that multiple Ni species can coexist, depending on the preparation conditions (calcination temperature, duration of calcination, Ni loading) [51–54]. It is generally known that NiO can already start interacting with Al_2O_3 at about 400 °C and that the amount and crystallinity of $NiAl_2O_4$ grows with increasing T_{calc} and t_{calc} [51].

The two NiO signals can be divided into a relatively sharp low temperature peak at 330–350 °C and a broad higher temperature peak at 420–460 °C. The low temperature NiO peak is assumed to stem from 3D printing with nickel ink which finely disperses small Ni particles onto the alumina support. This "surface NiO" (sNiO) is weakly bound and therefore easily reducible at temperatures below 350 °C. The second broad peak is matched to bulk nickel oxide (bNiO). Comparison of the TPR signals in Fig. 9a and b confirms the prevalence of sNiO by nickel ink deposition via binder jetting in contrast to conventionally wet impregnated samples. Table 3 lists the fraction of present Ni species determined by peak fitting of the TPR signal and reveals that sNiO represents 26–30 % of NI samples whereas WI samples contain half of the amount of sNiO (WI_c450) or even none (WI_c600). The set of two broad reduction peaks above 780 °C match the reduction temperature of nickel aluminate species since sufficient energy is provided for integration of Ni ions into the alumina lattice. Analogous to NiO, the signal at 780–830 °C could stem from weakly bound $NiAl_2O_4$ and the high temperature peak at 910–940 °C results from bulk crystalline $NiAl_2O_4$. TPR profiles of $NiAl_2O_4$ featuring two high-temperature peaks were reported before [55–58]. Furthermore, pure bulk NiO and $NiAl_2O_4$ were additionally analyzed by TPR as reference (see Supporting Information, Fig. S3) and confirm the presented regions of reduction temperature in Fig. 9a and b. The bulk reference samples only feature the reduction peaks for bNiO and bulk $NiAl_2O_4$ at about 550 °C and 900 °C, respectively and therefore confirm the presence of surface Ni species with facilitated reduction behavior when catalysts are prepared by NI. Nevertheless, with a fraction of about 60 %, nickel aluminate is overall predominantly formed in contrast to nickel oxide.

Table 3

Ni loading w_{Ni}, degree of reduction R_{TPR} of NI and WI samples determined by TPR analysis weight percentage of nickel oxide (surface NiO: sNiO, bulk NiO: bNiO) and Ni aluminate determined by peak fitting of H_2 consumption determined by TPR.

Sample	w_{Ni} (wt.%)	R_{TPR} (%)	NiO (wt.%)	sNiO (wt.%)	bNiO (wt.%)	$NiAl_2O_4$ (wt.%)
NI_i_c600	3.0	108	43	28	15	65
NI_d_c600	3.5	100	43	28	14	57
WI_c600	2.5	99	17	0	17	82
WI_c450	2.4	95	22	12	10	73

Although the NI samples differ in post-processing stage (d/i), the ratio of NiO to $NiAl_2O_4$ unchangingly approximates 40:60 (see Table 3), indicating that under the studied conditions, NI binder jetting generates Ni/Al_2O_3 catalysts with a consistent Ni species composition. The different post-processing conditions shift the TPR signals of the NI catalysts as shown in Fig. 9a. Comparing NI_i_c600 and NI_d_c600, infiltration shifts the reduction temperature to higher temperatures. Since the in situ impregnation with Ni nitrate containing ink facilitates fine dispersion of nickel (as shown with XPS), and a low Ni loading, nickel aluminate is formed easily, even at relatively low T_{calc} which would normally yield less spinel phase [59].

4. Conclusion

This work advances heterogeneous catalyst preparation by introduction of a fabrication method for supported nickel catalysts utilizing the powder-based AM technique binder jetting. Preliminary tests provided a proof of concept for the feasibility of printing mechanically stable Al_2O_3-supported Ni catalysts via BJ where the nickel precursor is directly integrated into the printing process, therefore omitting a

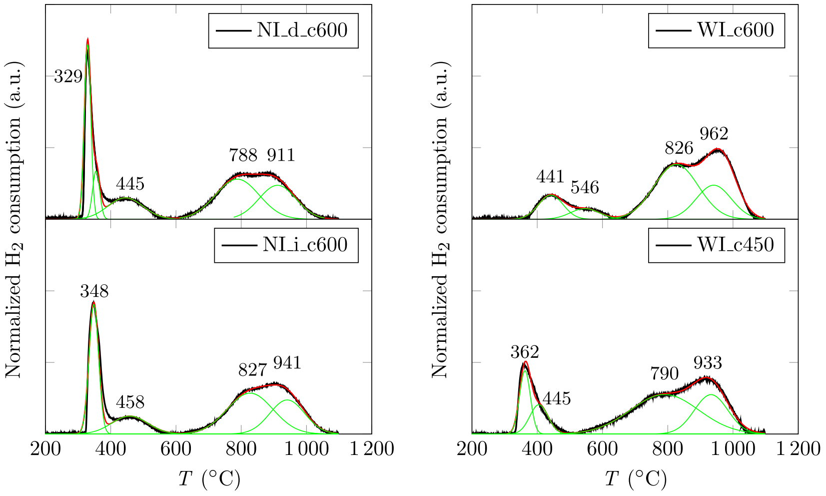

(a) Nickel ink deposition (NI)

(b) Wet impregnation (WI)

Fig. 9. TPR profiles with normalized H_2 consumption of (a) catalysts printed by nickel ink deposition (NI) after infiltration/debindering (i/d) and calcination at different temperatures (c450/c600), and (b) wet impregnation (WI), calcined at different temperatures (c450/c600).

subsequent impregnation step.

The 3D printed catalysts were characterized thoroughly using XPS, XAS and TPR. All three methods complemented each other by providing insights into the simultaneous formation of NiO and $NiAl_2O_4$ with varying ratios considering the underlying preparation conditions such as the preparation method (NI/WI) and thermal preparation conditions. NI generated Ni catalysts with similar characteristics as conventionally wet impregnated samples prepared under comparable conditions. Due to Ni loadings of max. 3.5 wt.%, facilitated incorporation of nickel into the alumina support resulted in the formation of about 60 wt.% nickel aluminate spinel for in situ impregnated catalysts printed by BJ. XPS analysis evidenced a finer nickel dispersion using the NI method than wet impregnation due to the deposition of nickel nitrate through fine printhead nozzles onto the alumina powder. Moreover, a superior CO_2 hydrogenation activity using NI catalysts was observed in comparison to WI catalysts treated under the same thermal conditions. The post-processing infiltration step, which distinguishes the preparation from conventional ones, covers active centers after nickel immobilization by introduction of alumina particles and aggravates reduction, observable by XPS, XAS and TPR.

This proof of concept enables further developments regarding the usage of AM in catalyst preparation, especially by incorporating catalyst precursor into the printing liquid in the context of BJ. A potential advancement is the usage of more than one metal salt solution to yield multi-metal catalysts by multi-component in situ impregnation. In addition, the nickel loading could be improved by repeated deposition of Ni ink onto a single powder layer or increasing the amount of metal per layer by process parameter optimization. Investigating the point of zero charge (PZC) may offer valuable insights into the interaction between the ink and (transition) alumina surface, leading to enhanced metal dispersion. Moreover, this knowledge could aid in optimizing the selection of material feedstock for 3D printing. At a later development stage, it becomes pertinent to conduct long-term stability tests to enhance catalyst performance and gain insights into its deactivation behavior.

CRediT authorship contribution statement

Hanh My Bui: Conceptualization, Methodology, Formal-analysis, Investigation, Visualization, Writing-original-draft, Writing-review-editing. **Tim Kratky:** Investigation, Formal-analysis, Writing-original-draft, Writing-review-editing. **Insu Lee:** Investigation, Formal-analysis. **Rachit Khare:** Investigation. **Max Hiller:** Investigation. **Steffen Wedig:** Investigation. **Sebastian Günther:** Writing-original-draft. **Olaf Hinrichsen:** Supervision, Project-administration, Funding-acquisition, Writing-review-editing.

Declaration of Competing Interest

The authors declare that they have no known competing financial interests or personal relationships that could have appeared to influence the work reported in this paper.

Data availability

Data will be made available on request.

Acknowledgements

H.M. Bui acknowledges the support of the TUM Graduate School. The authors acknowledge DESY beamline P-65 (Hamburg, Germany), a member of the Helmholtz Association HGF, for the provision of experimental facilities and beamtime for X-ray experiments. Furthermore, the authors thank Florian Zahn and Lennart Wahl for the support during the beamline measurements in Hamburg. Additionally, H.M. Bui would like to thank Christoph Gross for providing the facilities for sample reduction.

Appendix A. Supplementary data

Supplementary data associated with this article can be found, in the online version, at https://doi.org/10.1016/j.catcom.2023.106738.

References

[1] M. Komiyama, Design and Preparation of Impregnated Catalysts, Catal. Rev. 27 (1985) 341–372.

[2] A. Afshar Taromi, S. Kaliaguine, Hydrodeoxygenation of triglycerides over reduced mesostructured Ni/γ-alumina catalysts prepared via one-pot sol-gel route for green diesel production, Appl. Catal. A: General 558 (2018) 140–149.

[3] Y.-J. Huang, J.A. Schwarz, J.R. Diehl, J.P. Baltrus, Effect of Catalyst Preparation on Catalytic Activity, Appl. Catal. 36 (1988) 163–175.

[4] M. Romero-Sáez, A.B. Dongil, N. Benito, R. Espinoza-González, N. Escalona, F. Gracia, CO_2 methanation over nickel-ZrO_2 catalyst supported on carbon nanotubes: A comparison between two impregnation strategies, Appl. Catal. B: Environ. 237 (2018) 817–825.

[5] Y.-L. Lee, B.-J. Kim, H.-R. Park, S.-Y. Ahn, K.-J. Kim, H.-S. Roh, Customized Ni–MgO–Al_2O_3 catalyst for carbon dioxide reforming of coke oven gas: Optimization of preparation method and co-precipitation pH, J. CO2 Util. 42 (2020), 101354.

[6] M. Yusuf, A. Salaam Farooqi, M. Azad Alam, L. Kok Keong, K. Hellgardt, B. Abdullah, Performance of Ni/Al_2O_3-MgO catalyst for Dry Reforming of Methane: Effect of preparation routes, IOP Conf. Ser.: Mater. Sci. Eng. 1092 (2021), 012069.

[7] G. Li, L. Hu, J.M. Hill, Comparison of reducibility and stability of alumina-supported Ni catalysts prepared by impregnation and co-precipitation, Appl. Catal. A: General 301 (2006) 16–24.

[8] S. Ewald, M. Kolbeck, T. Kratky, M. Wolf, O. Hinrichsen, On the deactivation of Ni-Al catalysts in CO_2 methanation, Appl. Catal. A: General 570 (2019) 376–386.

[9] J. Regalbuto, Catalyst Preparation: Science and Engineering, Taylor & Francis, Hoboken, 2007.

[10] V.G. Baldovino-Medrano, M.T. Le, I. van Driessche, E. Bruneel, C. Alcázar, M. T. Colomer, R. Moreno, A. Florencie, B. Farin, E.M. Gaigneaux, Role of shaping in the preparation of heterogeneous catalysts: Tableting and slip-casting of oxidation catalysts, Catal. Today 246 (2015) 81–91.

[11] P. Munnik, P.E. de Jongh, K.P. de Jong, Recent developments in the synthesis of supported catalysts, Chem. Rev. 115 (2015) 6687–6718.

[12] J.M. Asua, B. Delmon, Theoretical study of the influence of nonuniform active-phase distribution on activity and selectivity of hydrodesulfurization catalysts, Ind. Eng. Chem. Res. 26 (1987) 32–39.

[13] E. Assaf, L. Jesus, J. Assaf, The active phase distribution in Ni/Al_2O_3 catalysts and mathematical modeling of the impregnation process, Chem. Eng. J. 94 (2003) 93–98.

[14] G.D. Wehinger, Improving the radial heat transport and heat distribution in catalytic gas-solid reactors, Chem. Eng. Process. - Proc. Intensif. 177 (2022), 108996.

[15] M. Bracconi, Intensification of catalytic reactors: A synergic effort of Multiscale Modeling, Mach. Learn. Addit. Manufact. Chem. Eng. Process. - Process Intensif. 181 (2022), 109148.

[16] L.R. Rosseau, V. Middelkoop, H.A. Willemsen, I. Roghair, M. van Sint Annaland, Review on Additive Manufacturing of Catalysts and Sorbents and the Potential for Process Intensification, Front. Chem. Eng. 4 (2022).

[17] J. Zhu, P. Wu, Y. Chao, J. Yu, W. Zhu, Z. Liu, C. Xu, Recent advances in 3D printing for catalytic applications, Chem. Eng. J. 433 (2022), 134341.

[18] O.A. Alimi, R. Meijboom, Current and future trends of additive manufacturing for chemistry applications: a review, J. Mater. Sci. 56 (2021) 16824–16850.

[19] E. Bogdan, P. Michorczyk, 3D Printing in Heterogeneous Catalysis-The State of the Art, Materials 13 (2020) 4534.

[20] O.A. Alimi, C.A. Akinnawo, R. Meijboom, Monolith catalyst design via 3D printing: a reusable support for modern palladium-catalyzed cross-coupling reactions, New J. Chem. 44 (2020) 18867–18878.

[21] A. Davó-Quiñonero, D. Sorolla-Rosario, E. Bailón-García, D. Lozano-Castelló, A. Bueno-López, Improved asymmetrical honeycomb monolith catalyst prepared using a 3D printed template, J. Hazard. Mater. 368 (2019) 638–643.

[22] P. Michorczyk, E. Hedrzak, A. Wegrzyniak, Preparation of monolithic catalysts using 3D printed templates for oxidative coupling of methane, J. Mater. Chem. A 4 (2016) 18753–18756.

[23] F. Álvarez, A. Cifuentes, I. Serrano, L. Franco, G. Fargas, F. Fenollosa, R. Uceda, L. Llanes, C. Tardivat, J. Llorca, J.J. Roa, Optimization of the sintering thermal treatment and the ceramic ink used in direct ink writing of α-Al_2O_3: Characterization and catalytic application, J. Eur. Ceram. Soc. 42 (2022) 2921–2930.

[24] F. Car, G. Brnadić, V. Tomašić, D. Vrsaljko, Advanced preparation method of monolithic catalyst carriers using 3D-printing technology, Prog. Addit. Manufact. 7 (2022) 797–808.

[25] S. Hock, C. Rein, M. Rose, 3D–Printed Acidic Monolithic Catalysts for Liquid-Phase Catalysis with Enhanced Mass Transfer Properties, ChemCatChem 14 (2022).

[26] I. Lucentini, G. García Colli, C. Luzi, I. Serrano, L. Soler, N.J. Divins, O.M. Martínez, J. Llorca, Modelling and simulation of catalytic ammonia decomposition over Ni-Ru deposited on 3D-printed CeO_2, Chem. Eng. J. 427 (2022), 131756.

[27] Z. Yuan, L. Liu, W. Ru, D. Zhou, Y. Kuang, J. Feng, B. Liu, X. Sun, 3D printed hierarchical spinel monolithic catalysts for highly efficient semi-hydrogenation of acetylene, Nano Res. 15 (2022) 6010–6018.

[28] T. Li, J. Gonzalez-Gutierrez, I. Raguž, C. Holzer, M. Li, P. Cheng, M. Kitzmantel, L. Shi, L. Huang, Material extrusion additively manufactured alumina monolithic structures to improve the efficiency of plasma-catalytic oxidation of toluene, Addit. Manufact. 37 (2021), 101700.

[29] M. González-Castaño, F. Baena-Moreno, J. Carlos Navarro de Miguel, K.U. Miah, F. Arroyo-Torralvo, R. Ossenbrink, J.A. Odriozola, W. Benzinger, A. Hensel, A. Wenka, H. Arellano-García, 3D-printed structured catalysts for CO_2 methanation reaction: Advancing of gyroid-based geometries, Energy Convers. Manage. 258 (2022), 115464.

[30] K. Essa, H. Hassanin, M.M. Attallah, N.J. Adkins, A.J. Musker, G.T. Roberts, N. Tenev, M. Smith, Development and testing of an additively manufactured monolithic catalyst bed for HTP thruster applications, Appl. Catal. A: General 542 (2017) 125–135.

[31] J. Liu, Y. Gao, Y. Fan, W. Zhou, Fabrication of porous metal by selective laser melting as catalyst support for hydrogen production microreactor, Int. J. Hydrogen Energy 45 (2020) 10–22.

[32] T. Ludwig, J. Seckendorff, C. Troll, R. Fischer, M. Tonigold, B. Rieger, O. Hinrichsen, Additive Manufacturing of Al_2O_3–Based Carriers for Heterogeneous Catalysis, Chem. Ing. Tech. 90 (2018) 703–707.

[33] H.M. Bui, R. Fischer, N. Szesni, M. Tonigold, K. Achterhold, F. Pfeiffer, O. Hinrichsen, Development of a manufacturing process for Binder Jet 3D printed porous Al_2O_3 supports used in heterogeneous catalysis, Addit. Manufact. 50 (2022), 102498.

[34] H.M. Bui, P.F. Großmann, T. Gros, M. Blum, A. Berger, R. Fischer, N. Szesni, M. Tonigold, O. Hinrichsen, 3D printed co-precipitated Ni-Al CO_2 methanation catalysts by Binder Jetting: Fabrication, characterization and test in a single pellet string reactor, Appl. Catal. A: General 643 (2022), 118760.

[35] S. Timoshenko, J.N. Goodier, Theory of elasticity, second ed., McGraw-Hill, 1951.

[36] DIN EN 623–2:1993–11, Hochleistungskeramik; Monolithische Keramik; Allgemeine und strukturelle Eigenschaften; Teil 2: Bestimmung von Dichte und Porosität, 1993.

[37] Y.-B.P. Kwan, J.R. Alcock, The impact of water impregnation method on the accuracy of open porosity measurements, J. Mater. Sci. 37 (2002) 2557–2561.

[38] B. Ravel, M. Newville, ATHENA, ARTEMIS, HEPHAESTUS: data analysis for X-ray absorption spectroscopy using IFEFFIT, J. Synchrotron Radiat. 12 (2005) 537–541.

[39] D. Monti, Temperature-programmed reduction. Parametric sensitivity and estimation of kinetic parameters, J. Catal. 83 (1983) 323–335.

[40] K. Mocala, A. Navrotsky, Structural and Thermodynamic Variation in Nickel Aluminate Spinel, J. Am. Ceram. Soc. 72 (1989) 826–832.

[41] R. Lindner, Å. Åkerström, Selbstdiffusion und Reaktion in Oxyd- und Spinellsystemen, Z. für Phys. Chem. 6 (1956) 162–177.

[42] F.S. Pettit, E.H. Randklev, E.J. Felten, Formation of $NiAl_2O_4$ by Solid State Reaction, J. Am. Ceram. Soc. 49 (1966) 199–203.

[43] H.L. Rotgerink, H. Bosch, J.G. van Ommen, J. Ross, The effect of Ni-Al ratio on the properties of coprecipitated nickel-alumina catalysts with high nickel contents, Appl. Catal. 27 (1986) 41–53.

[44] T. Burger, H.M.S. Augenstein, F. Hnyk, M. Döblinger, K. Köhler, O. Hinrichsen, Targeted Fe–Doping of Ni–Al Catalysts via the Surface Redox Reaction Technique for Unravelling its Promoter Effect in the CO_2 Methanation Reaction, ChemCatChem 12 (2020) 649–662.

[45] J.H. Kwak, L. Kovarik, J. Szanyi, CO_2 Reduction on Supported Ru/Al_2O_3 Catalysts: Cluster Size Dependence of Product Selectivity, ACS Catal. 3 (2013) 2449–2455.

[46] H.C. Wu, Y.C. Chang, J.H. Wu, J.H. Lin, I.K. Lin, C.S. Chen, Methanation of CO_2 and reverse water gas shift reactions on Ni/SiO_2 catalysts: the influence of particle size on selectivity and reaction pathway, Catal. Sci. Technol. 5 (2015) 4154–4163.

[47] J.K. Kesavan, I. Luisetto, S. Tuti, C. Meneghini, G. Iucci, C. Battocchio, S. Mobilio, S. Casciardi, R. Sisto, Nickel supported on YSZ: The effect of Ni particle size on the catalytic activity for CO_2 methanation, J. CO2 Util. 23 (2018) 200–211.

[48] S. Loiha, W. Klysubun, P. Khemthong, S. Prayoonpokarach, J. Wittayakun, Reducibility of Ni and NiPt supported on zeolite beta investigated by XANES, J. Taiwan Inst. Chem. Eng. 42 (2011) 527–532.

[49] P. Lu, T. Teranishi, K. Asakura, M. Miyake, N. Toshima, Polymer-Protected Ni/Pd Bimetallic Nano-Clusters: Preparation, Characterization and Catalysis for Hydrogenation of Nitrobenzene, J. Phys. Chem. B 103 (1999) 9673–9682.

[50] J. Rynkowski, D. Rajski, I. Szyszka, J.R. Grzechowiak, Effect of platinum on the hydrogenation activity of nickel catalysts, Catal. Today 90 (2004) 159–166.

[51] J. Zieliński, Morphology of nickel/alumina catalysts, J. Catal. 76 (1982) 157–163.

[52] J. Zieliński, Effect of alumina on the reduction of surface nickel oxide; morphology of the surfaces of the surfaces of Ni/Al_2O_3 catalysts, J. Mol. Catal. 83 (1993) 197–206.

[53] B. Mile, D. Stirling, M.A. Zammitt, A. Lovell, M. Webb, The location of nickel oxide and nickel in silica-supported catalysts: Two forms of 'NiO' and the assignment of temperature-programmed reduction profiles, J. Catal. 114 (1988) 217–229.

[54] C. Li, Y.-W. Chen, Temperature-programmed-reduction studies of nickel oxide/alumina catalysts: effects of the preparation method, Thermochim. Acta 256 (1995) 457–465.

[55] J.H. Cho, S.H. An, T.-S. Chang, C.-H. Shin, Effect of an Alumina Phase on the Reductive Amination of 2-Propanol to Monoisopropylamine Over Ni/Al_2O_3, Catal. Lett. 146 (2016) 811–819.

[56] A. Morales-Marín, J.L. Ayastuy, U. Iriarte-Velasco, M.A. Gutiérrez-Ortiz, Nickel aluminate spinel-derived catalysts for the aqueous phase reforming of glycerol: Effect of reduction temperature, Appl. Catal. B: Environ. 244 (2019) 931–945.

[57] J.L. Rogers, M.C. Mangarella, A.D. D'Amico, J.R. Gallagher, M.R. Dutzer, E. Stavitski, J.T. Miller, C. Sievers, Differences in the Nature of Active Sites for Methane Dry Reforming and Methane Steam Reforming over Nickel Aluminate Catalysts, ACS Catal. 6 (2016) 5873–5886.

[58] L. Zhou, L. Li, N. Wei, J. Li, J.-M. Basset, Effect of $NiAl_2O_4$ Formation on Ni/Al_2O_3 Stability during Dry Reforming of Methane, ChemCatChem 7 (2015) 2508–2516.

[59] Y. Cesteros, P. Salagre, F. Medina, J.E. Sueiras, Preparation and Characterization of Several High-Area $NiAl_2O_4$ Spinels, Study Reducibility Chem. Mater. 12 (2000) 331–335.